Bulletin of the Seismological Society of America, 90, 3, pp. 616–628, June 2000

The Three-Dimensional Dynamics of Dipping Faults

by David D. Oglesby,* Ralph J. Archuleta, and Stefan B. Nielsen†

Abstract Recent two-dimensional dynamic simulations of dip-slip faulting (Nielsen, 1998; Oglesby *et al.,* 1998, 2000; Shi *et al.,* 1998) have shown that the asymmetric geometry of dip-slip faults that intersect the free surface can have large effects on the dynamics of earthquake rupture. The nonvertical dip angle of such faults leads to larger motion on the footwall than the hanging wall, as well as much larger motion from thrust/reverse faults than from normal faults with the same geometry and stress magnitudes. In the present work we perform full three-dimensional simulations of thrust/reverse, normal, and strike-slip faults, and show that the same effects exist in three dimensions. Strike-slip fault motion is either in between or lower than the motion of both dip-slip faults. Additional three-dimensional effects include strong rake rotation at the free surface. The results confirm the findings of the previous studies and further elucidate the dynamic effects of the free surface on fault rupture, slip, and ground motion. They are also borne out by early analyses of the 1999 Chi-Chi (Taiwan) thrust earthquake, which displayed higher motion on the hanging wall than on the footwall, and a strong oblique component of motion at the surface.

Introduction

Recently, much seismological research has focused on the investigation of fault dynamics. However, due to computational and theoretical constraints, most simulations of dynamic earthquake rupture have been limited to faults with a high degree of symmetry, such as faults in homogeneous whole spaces and vertical strike-slip faults. Much can be learned from such studies. However, there are both observational and theoretical arguments that the dynamics of faults with asymmetrical geometry are both qualitatively and quantitatively different from those of symmetrical faults. In particular, there is observational evidence that symmetry of ground motion with respect to fault-slip direction is lost when a fault does not have a vertical dip. Experimental foam rubber models of thrust/reverse and normal faults (Brune, 1996) have also shown this effect.

One of the effects of the loss of symmetry in the case of a dipping fault is that thrust/reverse faults may produce greatly amplified ground motion, particularly above the hanging wall near the fault trace. Allen *et al.* (1998) have shown evidence for such an effect in the 1971 San Fernando earthquake. They argue that strong vertical ground acceleration ($>$1 g) caused a section of road near the fault trace to decouple from the underlying ground, at which time the ground moved as much as 1.75 m horizontally beneath the road. Also, some studies have shown that thrust/reverse faults systematically produce higher ground motion than normal faults for equivalent magnitudes (McGarr, 1984; Cocco and Rovelli, 1989). Finally, there is also observational evidence that the motion of the hanging wall is larger than that of the footwall for dip-slip earthquakes (Nason, 1973; Steinbrugge *et al.,* 1975; Abrahamson and Somerville, 1996). It should be pointed out, however, that most statistical studies of thrust/reverse faulting do not separate out blind thrusts from faults that intersect the surface, and also suffer from a lack of near-source data. Since the near-source behavior of faults that intersect the surface is the subject of this study, there are few data points suitable for direct comparison. However, the 1999 Chi-Chi (Taiwan) earthquake, which occurred while this paper was under review, does provide a wealth of pertinent data for comparison and is discussed in the Conclusion.

Using the two-dimensional finite-element method, Oglesby *et al.* (1998, 2000) have shown that an asymmetry between thrust/reverse and normal faults can be caused by the interaction between the rupture process on the fault and the radiated stress field. Because of the asymmetric geometry of a nonvertical fault, seismic waves can be reflected off the free surface back onto the fault. Alternatively, this process can be thought of as an adjustment of the fault stress field to match the traction-free boundary condition of the free surface. The net effect of this process is to cause the normal stress on the fault to change from the value it that would

*Present address: Department of Geological Sciences, San Diego State University, 5500 Campanile Drive, San Diego, CA 92182-1020; *doglesby@moho.sdsu.edu*

†Present address: Istituto Nazionale di Geofisica, Dpto. di Scienze Fisiche, Universita di Napoli, Federico II, Via Cintia 45 (Monte S. Angelo), 80126 Napoli, Italy; *snielsen@na.infn.it*

have had if the earthquake had taken place either in a whole-space or on a vertical fault. The effect on the normal stress is opposite for thrust/reverse and normal faults, which results in an amplification of fault motion near the free surface for a thrust/reverse fault, and deamplification for a normal fault. An additional effect explored by Oglesby *et al.* (1998, 2000) and also noted by Brune (1996), Shi *et al.* (1998), and Brune and Anooshehpoor (1999) is that an asymmetry exists between hanging wall and footwall motion for a dipping fault. Oglesby *et al.* (1998, 2000) attribute this effect to the mass difference between the footwall and the hanging wall in the vicinity of the free surface. Brune (1996) and Shi *et al.* (1998) attribute this effect predominantly to waves trapped in the hanging wall. Both these dynamic effects are important, but a quasi-static effect of perhaps equal importance is that the points in the hanging wall are closer to the fault and thus experience a larger offset (Day, 1999, personal communication). This effect has been seen in the quasi-static antiplane dipping fault simulations of Davis and Knopoff (1991).

The current study extends the two-dimensional work of Oglesby *et al.* (1998, 2000) by using the three-dimensional finite-element method to simulate the dynamics of thrust/reverse, normal, and strike-slip faults. Although much insight may be gained with two-dimensional simulations, three-dimensional simulations provide greater insight into edge effects and more realistic wave attenuation and rupture front shapes. In particular, because a rupture front in three dimensions tends to be arc-shaped rather than linear, less energy is concentrated in the rupture front. This fact may diminish the free surface effects seen in two dimensions. Using the current method we investigate the effect of dip angle and slip direction on fault-rupture evolution and slip. We also examine the implications on ground motion.

Physical Model and Analytical Approach

The geometry for the current models is shown in Figure 1. We assume that the earthquake rupture initiates at depth and propagates up-dip at a velocity slower than that of the *S* waves. As previously mentioned, the radiated stress field must adjust itself to match the free surface stress boundary condition:

$$\left.\begin{aligned} \sigma_x^f &= 2\sigma_x \\ \sigma_y^f &= 0 \\ \sigma_{xy}^f &= 0 \end{aligned}\right\}, \tag{1}$$

where the superscripted quantities refer to the values of the stress in the presence of a free surface, and the superscriptless quantities refer to the values in a whole space. The second and third lines of equation (1) will approximately apply for any point within one-quarter radiation wavelength of the free surface, where the incident and reflected waves interfere in essentially the same manner as at the free surface. The

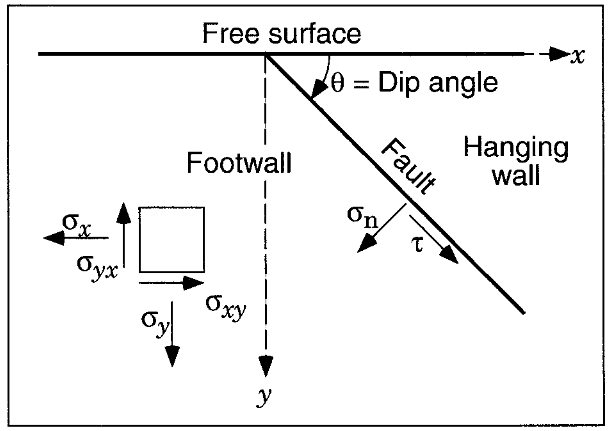

Figure 1. The geometry, coordinate system, and stress field of a nonvertical dip-slip fault.

doubling of the horizontal normal stress at the free surface is not true for a general location on the free surface. However, it can be shown via the static method of Crouch (1976) to be true for a point on the surface in the plane of a shear dislocation (Nielsen and Oglesby, in preparation). Assume that fault slip at depth would have caused a shear stress change of τ at this point in the absence of a free surface. This stress change corresponds to the stress build-up ahead of the crack tip that will eventually lead to rupture at this point. However, because of the presence of the free surface, the shear stress will be modified, and a normal stress increment will be induced. The expressions for the shear and normal stress increments are derived in Oglesby *et al.* (1998, 2000):

$$\begin{aligned} \Delta\tau &= -\tau \cos^2 2\theta \\ \Delta\sigma_n &= -4\tau \sin^3 \theta\cos\theta \end{aligned} \tag{2}$$

where θ is the fault-dip angle. Expressions similar to these were also derived for the specific case of a 45° dipping fault in Nielsen (1998). These stress increments are plotted as a function of dip angle in Figure 2. Notice that the shear stress increment $\Delta\tau$ will always be opposite to the direction of τ and thus reduces the magnitude of shear stress at that point. By itself, this effect brings the fault farther from its yield stress than it would have been in the absence of the free surface. However, the sign of the normal stress increment $\Delta\sigma_n$ will change depending on the sign of τ. Thus, for a thrust/reverse fault (τ positive in our sign convention), the normal stress increment is negative, corresponding to a compressional loading of the fault ahead of the crack tip as it approaches the free surface. Conversely, for a normal fault (τ negative), the normal stress increment is positive. This corresponds to a tensional unloading of the fault ahead of the crack tip. Thus, the change in normal stress will alter the yield stress in different ways for the different types of faults.

When the rupture front passes the point in question, the stress drops from the static to sliding frictional levels. Thus, the stress increments reverse sign: in the slipping region of the fault, the shear stress drops slightly less than it would have in the absence of a free surface, but in the normal stress there is an opposite effect for thrust/reverse and normal faults. The thrust/reverse fault will have a reduction in the magnitude of normal stress in the slipping region, and the normal fault will have an increase in normal stress amplitude. This asymmetry can lead to great differences in both fault motion and near-source ground motion. Ahead of the rupture front of a normal earthquake, the yield stress (equal to μ times the normal stress) can dip to the level of the shear-wave-stress peak. This effect can cause the rupture front to leap ahead to the surface, as is shown in Nielsen (1998) for the case of a 45° dipping fault. Likewise, the increased normal stress ahead of a thrust/reverse rupture front can act as a barrier to rupture at the free surface, leading to a greatly increased stress drop and thus amplified fault slip and ground motion. A dipping pure strike-slip fault, because it has no component of motion normal to the surface, will produce an earthquake stress field that does not have to rotate to match the free-surface-boundary condition. Thus although it may experience a modified shear stress due to reflections from the surface, it will experience no modification to the normal stress and produce ground motion that is symmetric with the direction of slip.

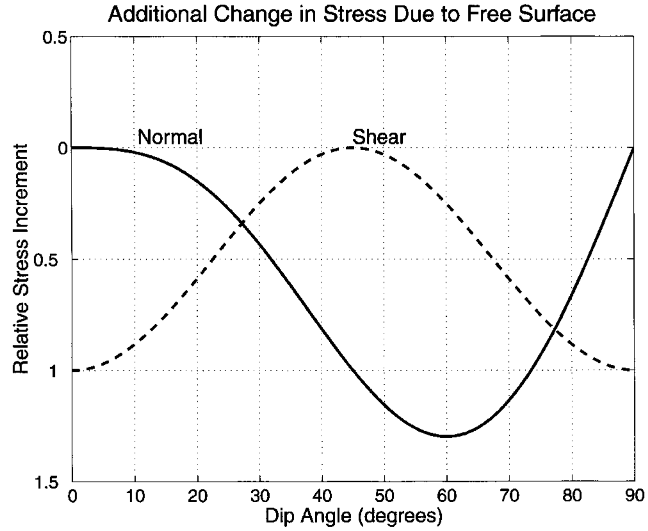

Figure 2. Stress changes on the fault induced by the presence of a free surface; shown as a function of dip angle. Solid line = $\Delta\sigma_n/\tau$, dashed line = $\Delta\tau/\tau$.

Table 1
Fault/Material Parameters

Fault width (down-dip)	28.28 km
Fault length (along strike)	20 km
Fault dip	30°, 45°, 60°
Shear prestress	14.14 bars
Normal prestress	26.52 bars
Static frictional coefficient	0.7
Sliding frictional coefficient	0.3
Density	3000 kg/m^3
Shear modulus	3×10^5 bars
Poisson's ratio	0.25
V_p	5.48 km/sec
V_s	3.16 km/sec

Table 2
Computational Parameters

Element size on fault	565.7 m × 500 m
Maximum frequency	~0.6 Hz
Critical slip time	1.2 sec

Simulation Method

We use the three-dimensional finite-element method (Whirley and Engelmann, 1993) to simulate the dynamics of normal, thrust/reverse, and strike-slip faults with dip angles of 30°, 45°, and 60°, with a particular focus on the 45° dip cases. The geometry of the faults is indicated schematically in Figure 1, and the fault, material, and computational parameters are given in Tables 1 and 2. Our fault friction law is given by

$$\begin{aligned} \tau &\leq \mu_s \sigma_n \quad \text{(for static friction)} \\ \tau &= \mu_d \sigma_n \quad \text{(for sliding friction)} \end{aligned} \tag{3}$$

where τ is the frictional shear stress, μ_s and μ_d are the static and sliding frictional coefficients, and σ_n is the normal stress across the fault. As in Oglesby *et al.* (1998, 2000), we use a slip time weakening law for the transition from μ_s to μ_d, corresponding to an effective slip-weakening distance of 1 to 20 cm, depending on the slip rate. The functional form of this friction law is that of a cosine with characteristic time of 1.2 sec, as is shown in Figure 3. The key feature of this friction law is that the frictional stress is directly proportional to the normal stress. Thus, the friction responds correctly to dynamic changes in normal stress induced by the free-surface interaction. The current fault-boundary condition precludes actual separation of the two sides of the fault. However, if the normal stress becomes tensile, the frictional stress is set to zero. This assumption partially accounts for the separation that would be expected from such an occurrence.

For simplicity and to isolate the purely geometrical effects, we use the same homogeneous prestress on all faults, with the only difference being the direction of shear stress. Rupture nucleation is achieved by temporarily applying a stress higher than the yield stress to a small region (<4 km^2) on each fault. Tests have shown that the results are insensitive to the method of rupture nucleation and only moderately sensitive to the exact position of nucleation. For the termination of slip, we use a simple slip-rate reversal healing method: When the fault slip-rate reverses direction (with re-

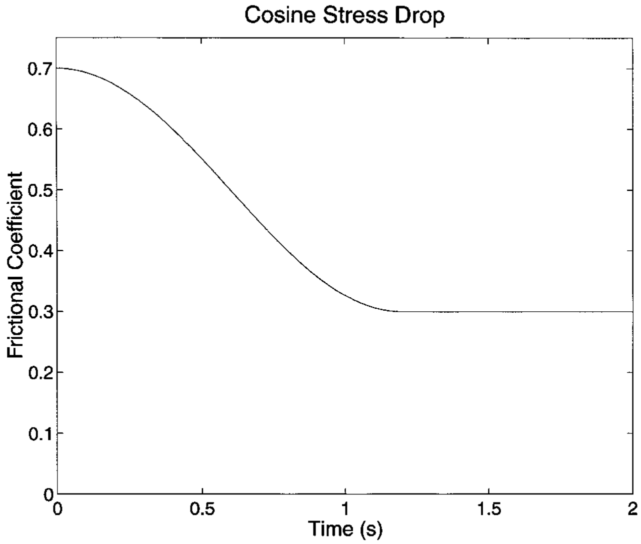

Figure 3. The law used for the reduction of the frictional coefficient μ from its static to its dynamic value. The form is that of a cosine function with a weakening time of 1.2 sec.

spect to the principal direction of slip), the fault is healed. No subsequent slip is allowed.

Simulation Results

Snapshots of hanging wall velocity for 45° thrust/reverse and normal faults are shown in Figures 4 and 5. Note that because of the asymmetry between hanging wall and footwall motion (to be explored in greater detail later in this article), the hanging wall velocity is not simply half the slip velocity. It can greatly exceed the footwall velocity in the vicinity of the free surface.

In all cases the fault nucleates at 22.6 km down-dip and 10 km along strike. By 3.0 sec the velocity in both the thrust/reverse and normal faults shows the pattern of a propagating elliptical crack. By 9.0 sec, the rupture front has swept out the lower section of the fault and is strengthening as it propagates toward the free surface. Up to this time, both faults display essentially identical slip-rate patterns because waves reflected from the free surface have not had the opportunity to affect the rupture dynamics; the faults have not yet "seen"

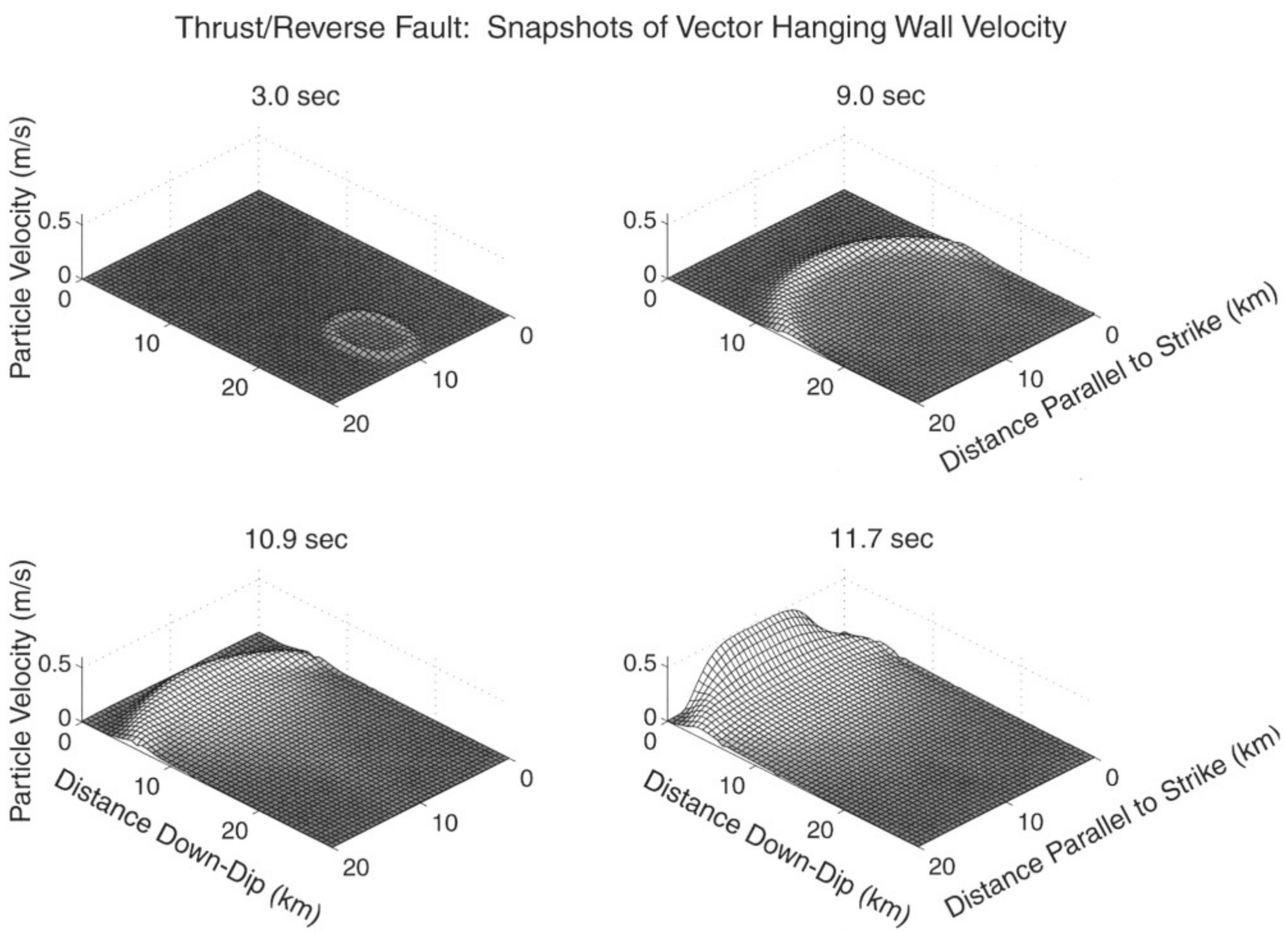

Figure 4. Snapshots of vector hanging wall velocity (on the fault plane) for the 45° dip thrust/reverse fault. Zero on the down-dip axis corresponds to the free surface. As the rupture front approaches the free surface, the particle velocities experience a great amplification due to the free surface interaction.

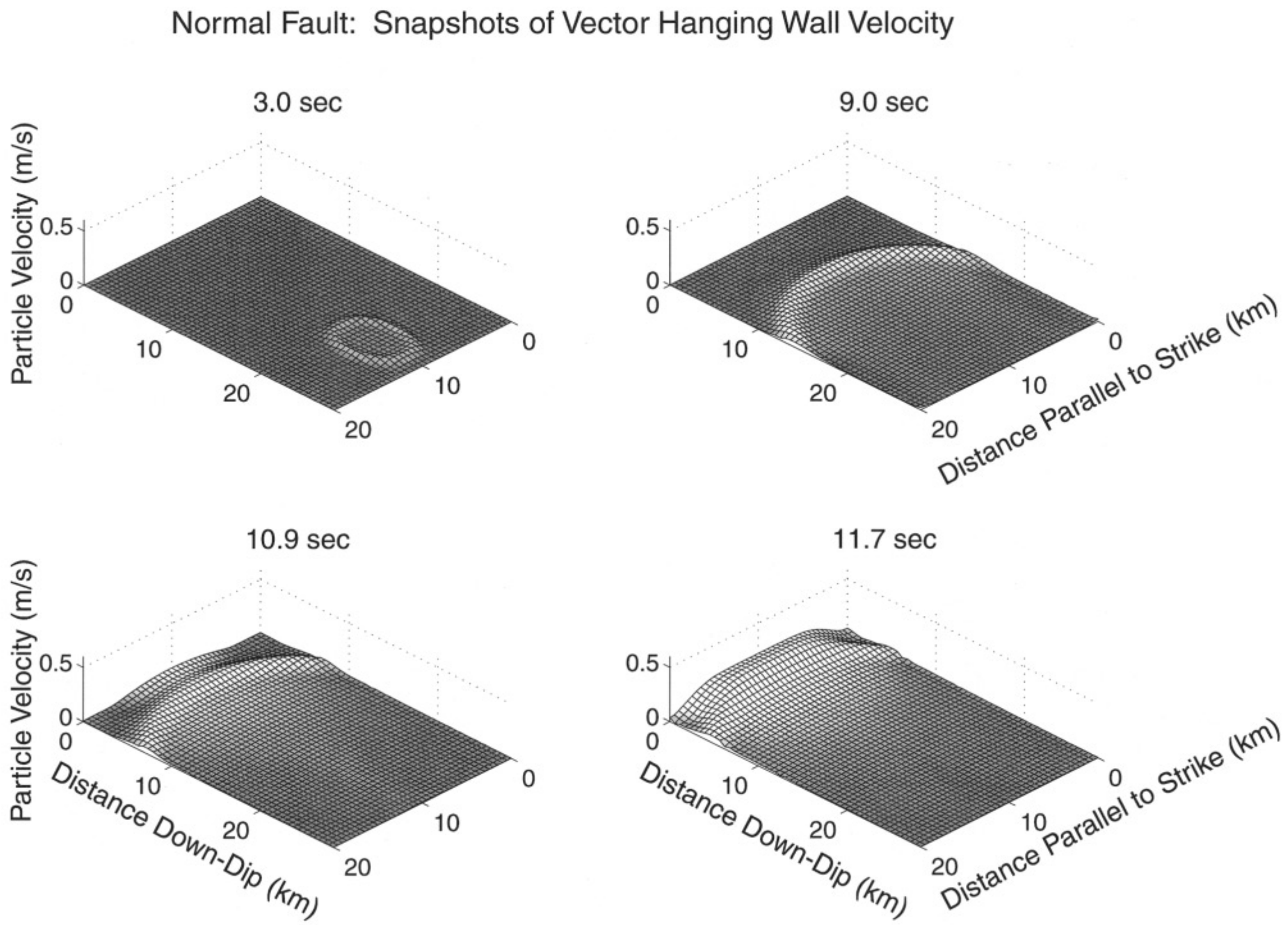

Figure 5. Snapshots of vector hanging wall velocity (on the fault plane) for the 45° dip normal fault. Zero on the down-dip axis corresponds to the free surface. Due to the free surface interaction, the rupture front has leaped ahead to the free surface by t = 10.9 sec.

the free surface. However, at 10.9 sec, the rupture front has almost reached the free surface, and the change in normal stress on the fault has started to have a noticeable effect on the rupture process. In the thrust/reverse case, the velocity just behind the rupture front has been greatly amplified. The normal fault has a smaller velocity than the thrust/reverse fault near the free surface. However, the largest difference between the two faults is that while the thrust/reverse fault rupture front has not yet reached the free surface at 10.9 sec, the normal fault is already slipping at the free surface. Although the main rupture front for the normal fault is still a small distance from the surface, a secondary rupture front has jumped ahead to the surface and already propagated back to meet the main front. This effect has been seen in two-dimensional simulations of dipping faults (Nielsen, 1998; Oglesby *et al.,* 1998, 2000). Finally, at 11.7 sec, both rupture fronts have reached the free surface. We see higher fault motion in the thrust/reverse fault (a stronger breakout phase) and lower fault motion in the normal fault. The amplified motion of the thrust/reverse fault and the deamplified motion of the normal fault have also been observed in the foam rubber models of Brune (1996) and Brune and Anooshehpoor (1999), the two-dimensional finite-element models of Oglesby *et al.* (1998, 2000) and in the two-dimensional lattice models of Zeng *et al.* (1997).

The strike-slip fault (Figure 6) shows a somewhat different rupture pattern due to the fact that the rupture front that propagates up-dip is largely mode III (antiplane) rather than mode II, as in the case of the thrust/reverse and normal faults. Mode II rupture can propagate at a higher speed than mode III (Burridge, 1973; Andrews, 1976), so in all cases the rupture front is an ellipse with its semi-major axis in the direction of mode II slip. Therefore, the strike-slip rupture front is elongated in the direction parallel to strike and travels more slowly toward the free surface than that of either the thrust/reverse or normal faults. As the rupture front approaches the free surface there is some amplification of the hanging wall velocity, but it is smaller than that of the thrust/reverse fault. There is no leaping ahead of the rupture front.

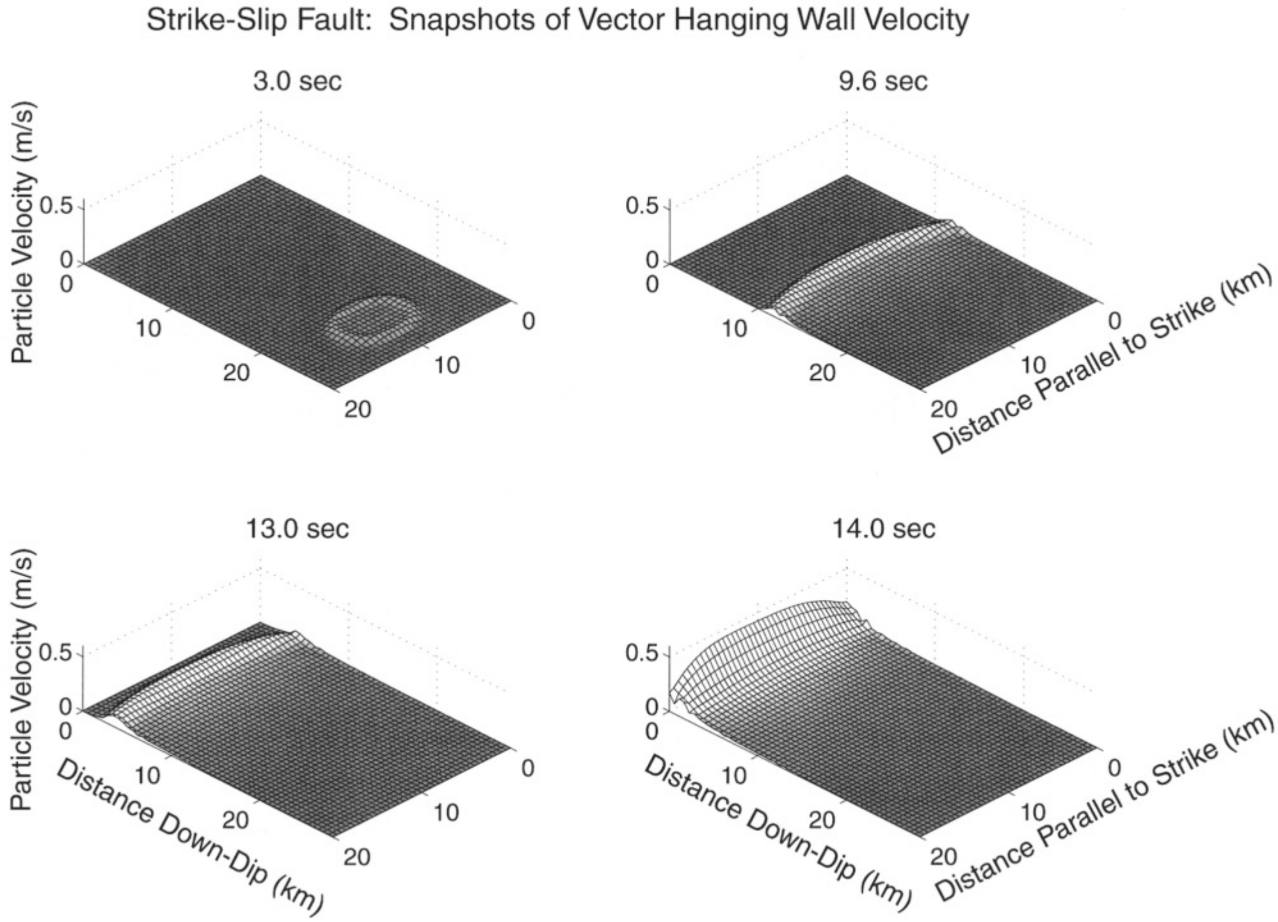

Figure 6. Snapshots of vector hanging wall velocity (on the fault plane) for the 45° dip strike-slip fault. Zero on the down-dip axis corresponds to the free surface. Because the slip is predominantly antiplane, the rupture front proceeds more slowly toward the free surface than in the dip-slip cases. There is less amplification of particle velocity than in the thrust/reverse case, but more than in the normal case.

It should be noted that in all cases there is amplification of particle motion as the rupture approaches the free surface, analogous to the well-known factor of 2 in seismic-wave amplitudes. This effect is also consistent with the vertical strike-slip fault models of Knopoff (1958) and Archuleta and Frazier (1978), and the quasi-static dip-slip fault models of Davis and Knopoff (1991) and Rudnicki and Wu (1995). The geometrical effect on the fault dynamics is to amplify the motion of thrust/reverse fault and deamplify the motion of the normal fault near the free surface relative to this already amplified level.

The source of this effect is easily seen by examining snapshots of the stress distributions on the 45° thrust/reverse, normal, and strike-slip faults at different times (Figure 7). At $t = 1.6$ sec, the thrust fault has just recently nucleated, so the shear-stress distribution is that of a propagating circular crack (which appears to be a bilateral crack in this one-dimensional slice of the fault). Because reflected stress waves from the free surface have not yet hit the fault, the solution is equivalent to that of a fault in a homogeneous whole space. At $t = 9.7$ sec, the reflected waves from the free surface have begun to manifest themselves by increasing the normal stress (directly proportional to the yield stress shown) ahead of the crack tip and decreasing the normal stress slightly behind it. At $t = 10.9$ sec, the rupture front has reached the free surface. At this point the crack tip must break through a greatly increased yield stress. Shortly thereafter, though, at $t = 12.0$ sec, the shear stress has dropped to a greatly decreased level (proportional to the now decreased normal stress) in agreement with the analytical solution. This amplified stress drop from an increased yield stress to a decreased sliding frictional stress is the cause of the higher slip rate seen in the rupture propagation snapshots.

The stresses on the 45° normal fault start out very similar to those of the thrust/reverse fault, prior to the arrival of reflected waves from the surface. However, at $t = 9.7$ sec, the yield stress is now reduced ahead of the crack tip, and increased behind it, in agreement with the analytical development. At $t = 10.4$ sec, the yield stress ahead of the rupture front has decreased to the point that it is exceeded by the shear-wave stress level. In this manner, a new rupture front is nucleated. This rupture front propagates bilaterally toward the free surface and back toward the primary rupture front. The effects of the rupture front jumping ahead were seen in the hanging wall velocity snapshots for the normal fault (Figure 5), when slip at the surface preceded the arrival of the main rupture front. Finally, at $t = 12.0$ sec, when the rupture has swept the entire fault, the sliding frictional level is slightly elevated due to the elevated normal stress. Because the stress level of the shear wave is lower than that of the initial stress and the sliding frictional stress is amplified, the stress drop near the free surface for a normal fault is much less than that of a thrust fault. The strongly deamplified stress drop leads to smaller fault motion. Additionally, the spreading of the rupture pulse between two rupture fronts causes the energy of the rupture to be spread out more in time, further weakening its effect. It should be noted that although the analytical development predicts a free surface effect on both the shear and normal stresses, for dip angles near 45°, the increment $\Delta\tau$ is almost zero. However, for dips of 30° and 60° as well, the free surface effect on normal stress dominates the dynamics.

The dominance of the time-dependent normal stress near the free surface is also shown by the lack of a strong free-surface effect on the stresses of the 45° dipping strike-slip fault. Because the motion of the strike-slip fault is parallel to the surface, the normal stress does not need to change to match the free-surface boundary condition. Thus, the normal stress remains unmodified throughout the simulation. There is no slip-direction-dependent amplification (right-lateral and left-lateral simulations are identical aside from a sign change).

The differences between the thrust/reverse, normal, and strike-slip faulting may also be seen by examining the peak particle motions on the hanging wall. Figures 8, 9, and 10 show surface plots of peak hanging wall velocity for the thrust/reverse, normal, and strike-slip faults. The down-dip component is largest for the thrust/reverse fault and smaller for the normal fault, in agreement with the previous results. Another interesting effect is the nontrivial strike-parallel velocity near the free surface of both the thrust/reverse and normal faults. This motion, in a direction perpendicular to the applied stress, corresponds to a rotation of rake in the vicinity of the free surface. Spudich (1992) has shown that dynamic stresses induced by fault rupture can be in a different direction than the static stresses. The degree of rake rotation depends on the ratio of the dynamic stress to the static stress, which can also be further amplified by rupture directivity. Since the dynamic stress changes described above are concentrated near the free surface, it is not surprising that rake rotation is most prominent in this location as well. The strike-slip fault, with its largely unaltered dynamic stresses, does not experience rake rotation to the same degree, as seen by its small down-dip velocity component.

As mentioned earlier, for all faults there is an asymmetry between hanging wall and footwall motions. This effect can been seen in Figure 11, which displays the peak-fault velocities and final displacements along a line running down-dip through the centers of the 30°, 45°, and 60° thrust/reverse, normal, and strike-slip faults. Near the free surface, the hanging walls for each type of fault have peak velocities and final displacements a factor of two or more higher than the footwalls. The asymmetry of roughly 4 in the case of the 30° dipping fault is consistent with the foam rubber results of Brune (1996). This asymmetry between footwall and hanging wall motion has also been noted in the two-dimensional dynamic simulations of Oglesby *et al.* (1998, 2000) and Shi *et al.* (1998). There are two important reasons for this asymmetry. First, the points in the hanging wall are closer to the fault (see Figure 1) and thus will experience a larger static offset than points in the footwall (Day, 1999, personal communication). This is a static effect seen in the quasi-static simulations of Davis and Knopoff (1991) and Rudniki and Wu (1995). An additional, dynamic reason for this asymmetry is the mass difference between the two sides of the fault near the free surface. The hanging wall wedge is much smaller than the footwall wedge. Thus for the same forces on both sides of the fault, the footwall will experience a greater acceleration. Additionally, trapped waves in the hanging wall may also contribute to the asymmetry between footwall and hanging wall motion (Shi *et al.,* 1998). The difference between hanging wall and footwall motion is largest for the 30° dipping fault, and smallest for the 60° dipping fault. This simple dependence on fault dip is to be expected because the hanging wall and footwall grow in geometrical similarity monotonically as the dip angle ranges from 0° to 90°.

We also see again that the peak velocity and final displacement of the thrust/reverse faults is larger than that of the normal faults by over 50%, with the motion of the strike-slip fault either in between these extremes or less than both dip-slip faults for most of the fault length. However, one interesting observation is that for the 30° dipping faults, the strike-slip fault has slightly higher peak velocity at the free surface than even the thrust/reverse fault. This effect is caused by both the angular dependence of the free-surface amplification and the mode of the rupture. As is seen in Figure 2, the 30° faults have a smaller normal stress increment than the 45° and 60° faults, so the free-surface amplification is least. The strike-slip fault, due to its predominantly mode III rupture, has a more linear (less arc-shaped) rupture front than the thrust fault near the free surface (compare Figures 4 and 6), so there is more energy hitting the free surface simultaneously. In all cases, the free-surface effects (hanging wall vs. footwall and style of faulting) on peak velocity decrease with down-dip distance because the deeply buried parts of the faults do not feel the effect of the free surface as strongly. However, the effects of the free surface do manifest themselves in the final displacements. This effect was also noted in the two-dimensional simula-

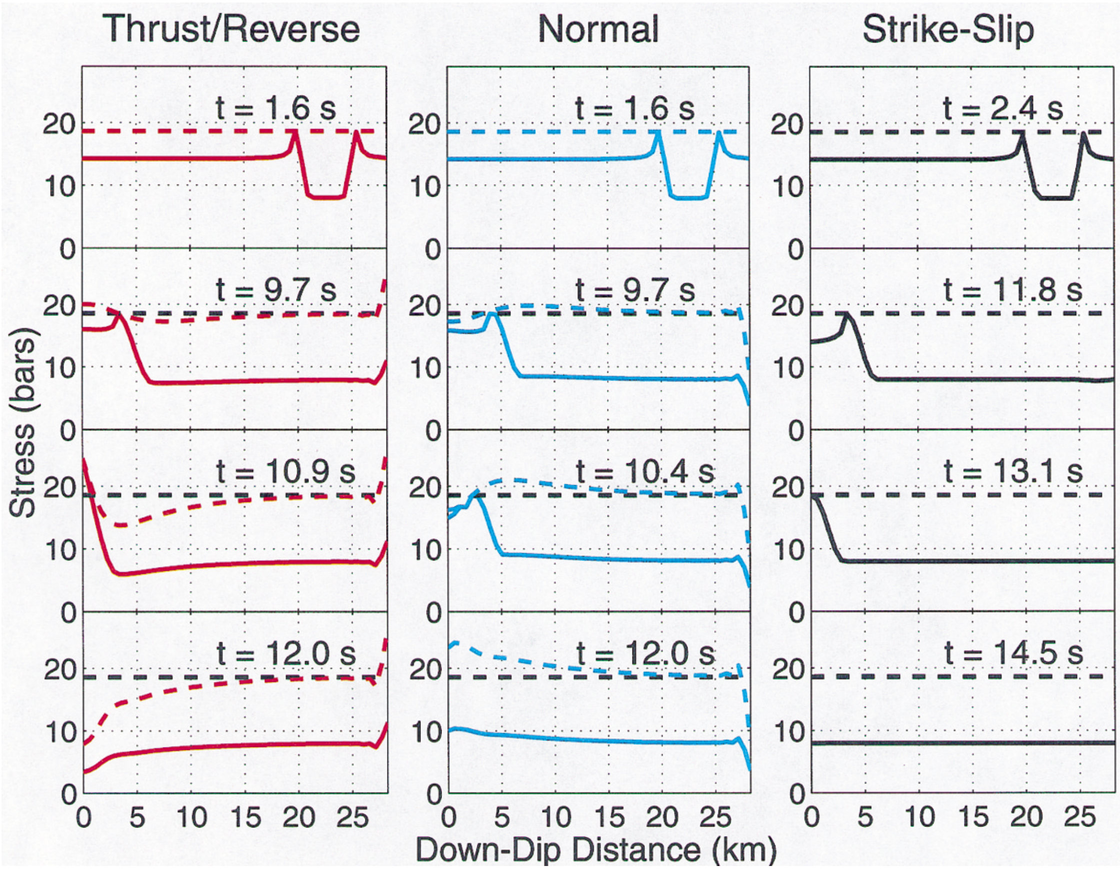

Figure 7. Snapshots of stresses along 45° dipping thrust, normal, and strike-slip faults during earthquake rupture. Values are shown for a line down the center of the fault plane at 10 km parallel to strike. Zero on the horizontal axis corresponds to the free surface, and 28.3 km on the horizontal axis corresponds to the down-dip edge of the fault. The solid curves denote shear stress, and the dashed curves denote yield stress. The black dashed line denotes the initial yield stress before dynamic stress modification.

tions of Oglesby *et al.* (1998) and is due to the fact that the breakout phase is the strongest pulse near the free surface; it is this pulse that causes the differences in peak fault velocity near the free surface. This pulse is not the largest phase at depth (the initial rupture pulse is larger), so it does not show up in the peak velocities in deeper parts of the faults. However, the breakout pulse still propagates down-dip on the faults and contributes to the final displacements everywhere. Thus, the final displacements display the free surface effects even in deeply buried parts of the fault.

Interestingly, all three faults experience some fault-normal velocity. Because the fault boundary condition precludes the opening of the fault, this motion corresponds to a translation or rotation of the fault itself. This effect is seen most obviously in the final fault-normal displacements (Figure 12). The thrust/reverse fault rotates clockwise a small amount with a pivot point at approximately 16 km down-dip. The normal fault rotates the opposite direction a slightly smaller amount. The strike-slip fault rotates about an axis perpendicular to that of the dip-slip faults, with a pivot point halfway along strike. This result agrees with the analytical results of Burridge (1973), except that the fault-normal motion is larger near the free surface.

The strong effect of the free surface on the fault motion also manifests itself with a large effect on the near-source ground motion. Figure 13 shows the peak vector (amplitude) particle velocity and final displacement for thrust/reverse, normal, and strike-slip faults with dips of 30°, 45°, and 60°. The ground motion is measured on a line bisecting the strike of the fault, going from the footwall to the hanging wall. For all dip angles, the peak particle velocity and final displacement near the fault is larger for the thrust/reverse fault than for the normal fault. The peak particle velocity and final displacement for the strike-slip fault either falls in between these extremes or is smallest overall, with the exception of the 30° dipping fault right at the fault trace. These results

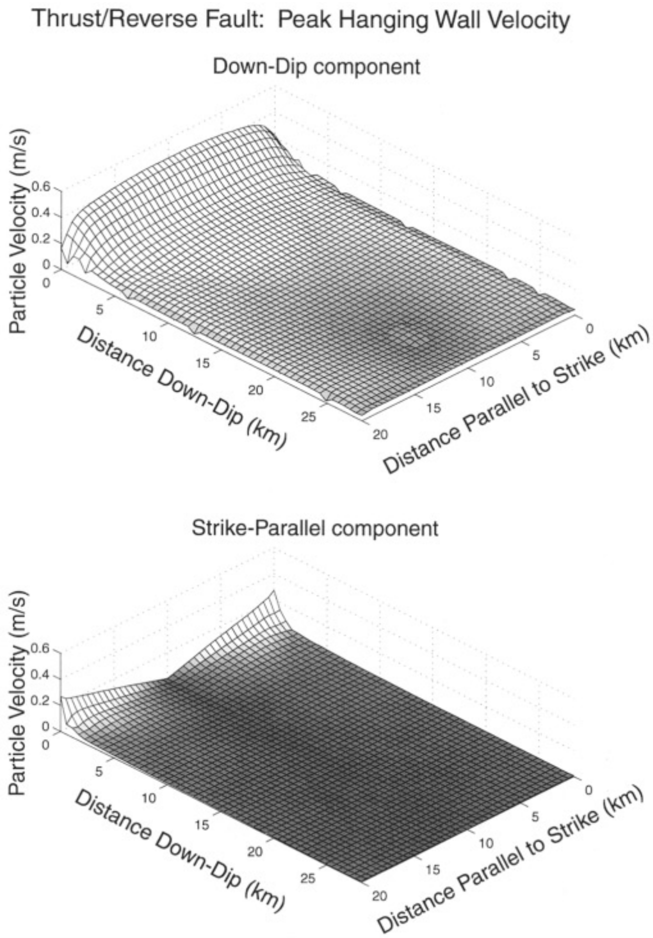

Figure 8. Peak absolute value of hanging wall velocity for the 45° dipping thrust/reverse fault. The coordinate system is the same as that of Figure 4. Note the large amplification near the free surface and the rake rotation at the upper corners of the fault.

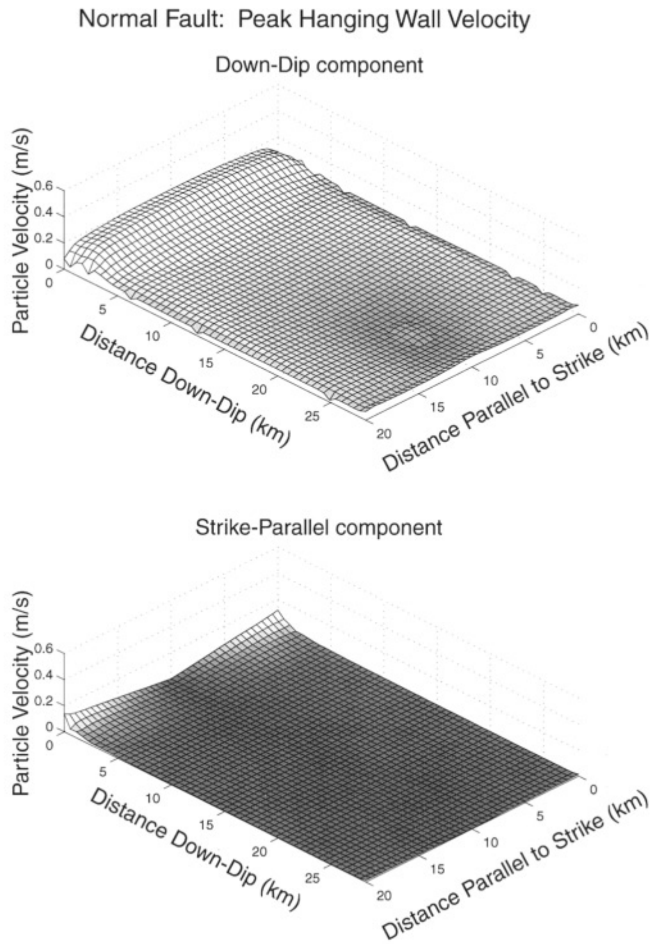

Figure 9. Peak absolute value of hanging wall velocity for the 45° dipping normal fault. The coordinate system is the same as that of Figure 4. There is much less amplification of fault motion near the free surface than in the case of the thrust/reverse fault. Rake rotation is similarly smaller.

agree with the two-dimensional results of Oglesby *et al.* (1998, 2000) and Brune and Anooshehpoor (1999) for the cases of the thrust/reverse and normal faults. Again, ground motion from right-lateral and left-lateral strike-slip motion is identical aside from the sign. The differences in near-source peak ground velocity between the different types of faults are a direct result of the stress-drop amplification of the thrust/reverse fault and the corresponding deamplification of the normal fault. The strike-slip fault, due to its different mode of rupture (III versus II for the dip-slip faults) has both a different rupture propagation pattern (as mentioned before) and a different radiation pattern, so it is difficult to compare directly to the dip-slip faults. Nevertheless, with its rake intermediate between the thrust/reverse and normal faults, it experiences no dynamic free-surface amplification or deamplification. Note that the difference between thrust/reverse and normal faulting does not simply decrease as the dip approaches 90°. These observations may be interpreted as being due to the competing effects of the free surface on dynamic shear and normal stress, which have different angular dependence (equation 2). A second feature of the ground motion is that there is a large discontinuity between the hanging wall and footwall motion for all types of faults. This effect is predominantly caused by the asymmetry in volume and mass on either side of the fault and is consistent with the difference between fault motion for the hanging wall and footwall mentioned earlier. It should be noted that the discontinuity in ground motion at the fault trace is in apparent conflict with attenuation relations such as Abrahamson and Somerville (1996), which have continuous distributions of ground motion over the surface. However, as Somerville (1999, personal communication) has pointed out, their model includes data from blind thrusts (which are shown in Oglesby *et al.,* 2000 to produce a spatially continuous ground motion) as well as faults that inter-

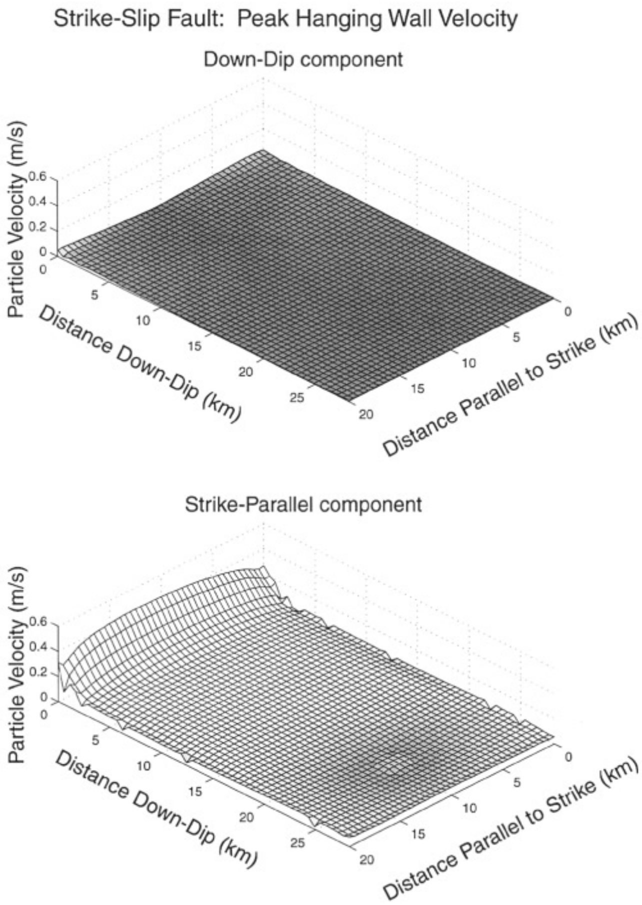

Figure 10. Peak absolute value of hanging wall velocity for the 45° dipping strike-slip fault. The coordinate system is the same as that of Figure 4. There is less amplification of fault motion near the free surface than in the case of the thrust/reverse fault. Rake rotation is minimal due to the small dynamic stresses near the free surface.

sect the surface, and there are few data points in the near-source region to allow differentiation between continuous and discontinuous models. Thus, the apparent conflict is likely due to both the lack of near-source data and the inclusion of data on faults of a different type than those simulated herein.

Conclusions

These three-dimensional results verify and extend our earlier two-dimensional work (Oglesby *et al.,* 1998, 2000). The simulations show that for the same initial stress magnitude, thrust/reverse faults can produce much higher fault and ground motion than normal faults. By performing three-dimensional simulations, we are furthermore able to simulate strike-slip faults that generally produce fault and ground motion either in between or less than the dip-slip faults. The difference between thrust/reverse and normal faulting is due to the asymmetric geometry of dip-slip faults with nonvertical dip angles and the resultant time-dependent normal stress on the fault. The time-dependent normal stress causes a feedback between the rupture and radiation processes. Simply stated, the reflected waves from the free surface amplify the motion of the thrust/reverse fault near the free surface and deamplify the motion of the normal fault. The comparison of the strike-slip fault motion is more complicated because of fundamental differences in radiation pattern and rupture-propagation speed. Additionally, the simulations show an asymmetry between hanging wall and footwall motion. We interpret this effect as being due to the volume and mass difference between the hanging wall and footwall near the free surface. Finally, the simulations show that high dynamic stresses near the free surface can lead to a strong strike-slip component of motion at the free surface even when the initial stresses are entirely dip-slip.

The results of the current study help to explain some observations concerning dip-slip faulting: (1) larger ground motion from thrust/reverse faults than normal faults, (2) larger ground motion on the hanging wall than on the footwall, and (3) oblique surface slip in primarily dip-slip earthquakes. They also match well with the physical foam-rubber models of Brune (1996) and Brune and Anooshehpoor (1999). The recent Chi-Chi (Taiwan) earthquake (which took place while this paper was under review) is an ideal test of the results of this study: It is a large thrust earthquake that ruptured through to the free surface, and for which there is much near-source data. Early analyses of strong-motion records (Shin *et al.,* 2000; Chung *et al.,* 2000), GPS data (Rau *et al.,* 1999), and mapped surface slip (Lee *et al.,* 1999), show that the hanging wall experienced far greater ground motion than the hanging wall (with a discontinuity in ground motion across the fault trace), and that there was a substantial left-lateral component of fault motion near the surface. The fact that observations of this event agree with the present fault models strongly implies that fault geometry (and in particular, the angle between the fault and the free surface) can have a very large effect on the gross characteristics of an earthquake of the type investigated in this study. The geometrical effects on the Chi-Chi earthquake will be explored in detail in a future publication (Oglesby and Day, in preparation).

The current results focus on the dynamic consequences of asymmetric fault geometry. They do not take into account other possible differences between thrust faults and normal faults (such as geological/tectonic setting and the average stress level). They also do not account for the fact that rock type may differ on either side of the fault, leading to additional asymmetry between hanging wall and footwall motion. Additionally, the approximations made in the current study (such as homogeneous structure and homogeneous stress fields) are clearly unrealistic for real faults. In particular, the static stress field and possibly the friction law itself may change in the upper few kilometers, leading to an overall decrease in fault motion. However, as pointed out in Og-

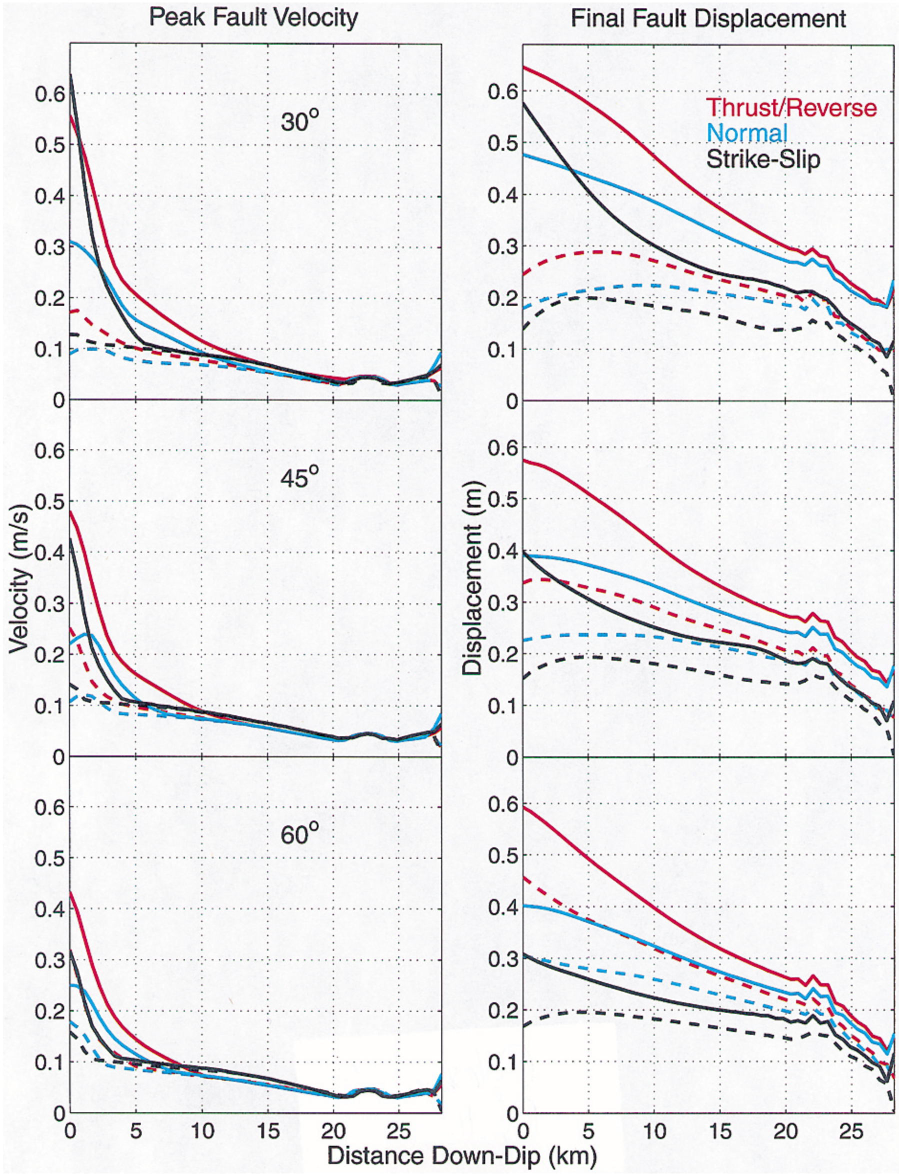

Figure 11. Comparison of absolute values of peak fault velocities and final displacements for 30°, 45°, and 60° thrust/reverse, normal, and strike-slip faults. Values are shown for a line down the center of the fault plane at 10 km parallel to strike. Zero on the horizontal axis corresponds to the free surface, and 28.3 km on the horizontal axis corresponds to the down-dip edge of the fault. Solid curves denote the hanging walls and dashed curves denote the footwalls. In all cases, the thrust/reverse faults have higher peak velocity than the normal faults, and hanging walls have higher peak velocity than footwalls. The displacement patterns are more complicated, as is the motion of the strike-slip fault.

lesby *et al.* (1998, 2000), inclusion of these features does not remove the asymmetry in ground motion. Finally, as also pointed out in Oglesby *et al.* (2000), the current results only apply for faults that reach the free surface—blind thrusts that are buried more than approximately one kilometer do not experience a strong free-surface effect.

Despite the limitations of such idealized simulations, the current work relaxes the common assumption of geometrical symmetry. It shows that fault geometry can contribute in a strongly nonlinear fashion to both fault rupture and nearby ground motion. Further relaxation of approximations may lead to further insight into the dynamics of faults in nature.

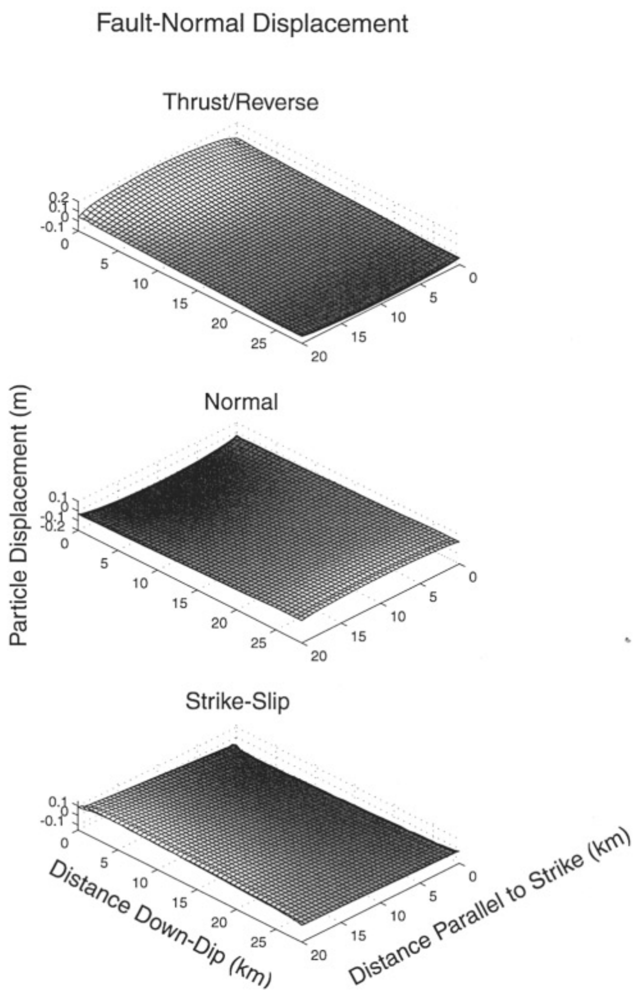

Figure 12. Comparison of final fault-normal displacements on the 45° dipping thrust/reverse, normal, and strike-slip faults. The sense of rotation agrees with the analytical solution of Burridge (1973), but there is an additional amplification of fault-normal motion near the free surface in all cases.

Acknowledgments

This research was supported by LLNL/IGPP Grant 98-GS012 and by the National Science Foundation under Grant EAR-9725709. Support for S. Nielsen was provided by the MRSEC Program of the National Science Foundation under Award No. DMR96-32716. The authors gratefully acknowledge useful conversations with Steve Day and Kim Olsen. This manuscript benefited greatly from insightful reviews by James Brune, Paul Somerville, and Michel Bouchon.

References

Abrahamson, N., and P. Somerville (1996). Effects of the hanging wall and footwall on ground motions recorded during the Northridge earthquake, *Bull. Seism. Soc. Am.* **86,** S93–S99.

Allen, C. R., J. N. Brune, L. S. Cluff, A. G. Barrows (1998). Evidence for unusually strong near-field ground motion on the hanging wall of the San Fernando fault during the 1971 earthquake, *Seism. Res. Lett.* **69,** 524–531.

Andrews, D. J. (1976). Rupture velocity of plane strain shear cracks, *J. Geophys. Res.* **81,** 5679–5687.

Archuleta, R. J. and G. A. Frazier (1978), Three-dimensional numerical simulations of dynamic faulting in a half-space, *Bull. Seism. Soc. Am.* **68,** 541–572.

Brune, J. (1996). Particle motions in a physical model of shallow angle thrust faulting, *Proc. Indian Acad. Sci. (Earth Planet. Sci.)* **105,** L197–L206.

Brune, J. N., and A. Anooshehpoor (1999). Dynamic geometrical effects on strong ground motion in a normal fault, *J. Geophys. Res.* **104,** 809–851.

Burridge, R. (1973). Admissible speeds for plane-strain self-similar shear cracks with friction but lacking cohesion, *Geophys. J. R. Astr. Soc.* **35,** 439–455.

Chung, J. K., T. C. Shin, F. T. Wu, R. Y. Chen, Y. M. Wu, C. S. Chang, and T. L. Teng (2000). Ground displacement around the fault of the September 20th, 1999, Chi-Chi Taiwan Earthquake, *Geophys. Res. Lett.* (submitted for publication).

Cocco, M., and A. Rovelli (1989). Evidence for the variation of stress drop between normal and thrust faulting earthquakes in Italy, *J. Geophys. Res.* **94,** 9399–9416.

Crouch, S. L. (1976). Solution of plane elasticity problems by the displacement discontinuity method, *Int. J. Numer. Meth. Engin.* **10,** 301–343.

Davis, P. M., and L. Knopoff (1991). The dipping antiplane crack, *Geophys. J. Int.* **106,** 581–585.

Knopoff, L. (1958). Energy release in earthquakes, *Geophys. J. R. Astr. Soc.* **1,** 44–52.

Lee, T., C. Cheng, and S. Hsu (1999). Fault rupture associated with the September 21, 1999 Chichi earthquake, West Central Taiwan, *AGU 1999 Fall Meeting Program,* 14.

McGarr, A. (1984). Scaling of ground motion parameters, state of stress, and focal depth, *J. Geophys. Res.* **89,** 6969–6979.

Nason, R. (1973). Increased seismic shaking above a thrust fault, in Murphy, ed.; *San Fernando, California, Earthquake of February 9, 1971,* L. Murphy (Editor), Vol. III, U.S. Dept. of Commerce/NOAA, 123–126.

Nielsen, S. B. (1998). Free surface effects on the propagation of dynamic rupture, *Geophys. Res. Lett.* **25,** 125–128.

Oglesby, D. D., R. J. Archuleta, and S. B. Nielsen (1998). Earthquakes on dipping faults: the effects of broken symmetry, *Science* **280,** 1055–1059.

Oglesby, D. D., R. J. Archuleta, and S. B. Nielsen (2000). The dynamics of dip-slip faulting: explorations in two dimensions, *J. Geophys. Res.* (in press).

Rau, R., J. Yu, T. Yu, M. Yang, and C. Tseng (1999). Co-seismic displacements of the 1999 Chi-Chi, Taiwan, earthquake sequence, AGU 1999 Fall Meeting Program, 14.

Rudniki, J., and M. Wu (1995). Mechanics of dip-slip faulting in an elastic half-space, *J. Geophys. Res.* **100,** 22,173–22,186.

Shi, B., A. Anooshehpoor, J. N. Brune, and Y. Zeng (1998). Dynamics of thrust faulting: 2D lattice model, *Bull. Seism. Soc. Am.* **88,** 1484–1494.

Shin, T. C., K. W. Kuo, W. H. Lee, T. L. Teng, and Y. B. Tsai (2000). A preliminary report on the 1999 Chi-Chi (Taiwan) earthquake, *Seism. Res. Lett.* (in press).

Spudich, P. (1992). On the inference of absolute stress levels from seismic radiation, *Tectonophysics* **211,** 99–106.

Steinbrugge, K., E. E. Scader, D. F. Moran (1975). Building damage in San Fernando Valley, in *San Fernando, California, Earthquake of 9 February 1971,* G. Oakeshott (Editor), CDMG Bulletin 196, 323–353.

Whirley, R. G., and B. E. Engelmann (1993). *DYNA3D: A Nonlinear, Explicit, Three-Dimensional Finite Element Code for Solid and Structural Mechanics: User Manual.* University of California, Lawrence Livermore National Laboratory, UCRL-MA-1107254 Rev. 1.

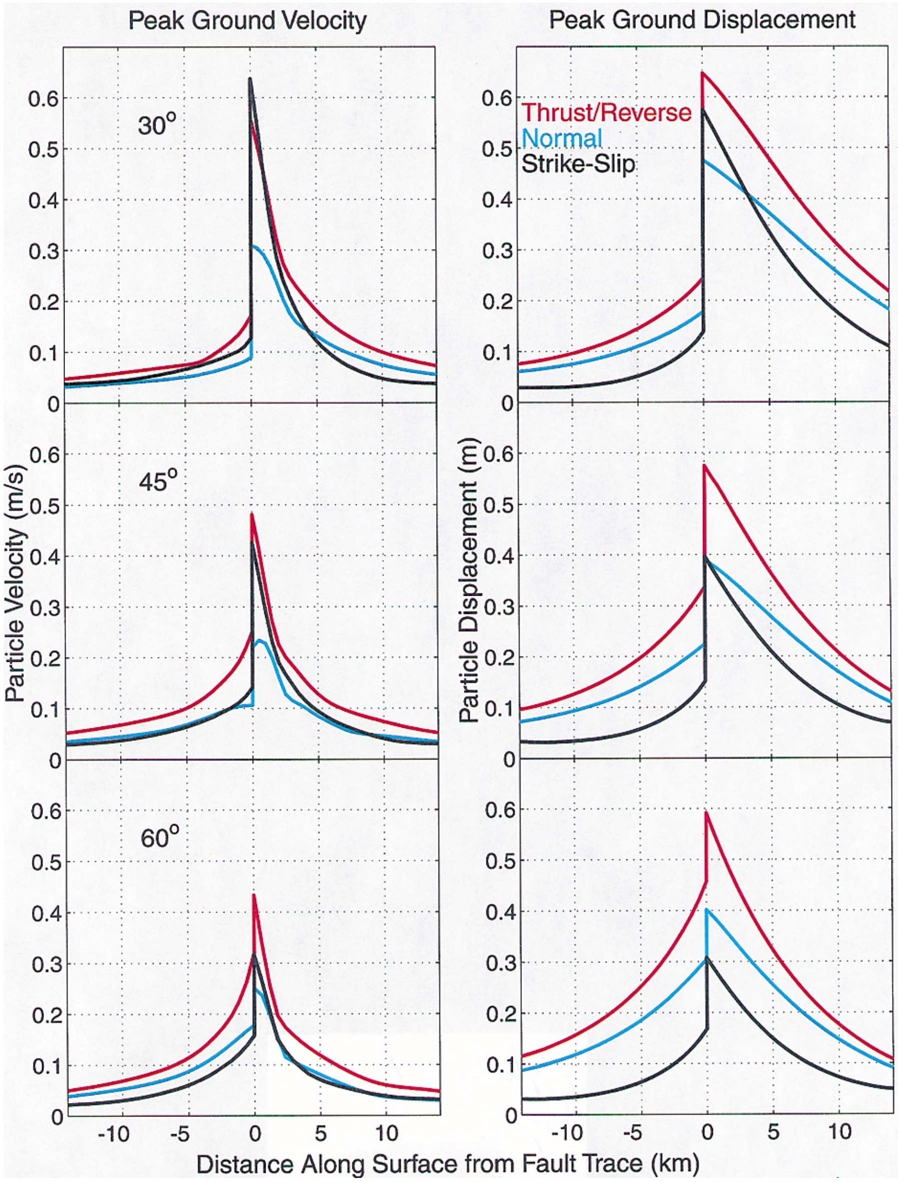

Figure 13. Comparison of peak absolute ground velocity and displacement for 30°, 45°, and 60° thrust/reverse, normal, and strike-slip faults. Values are shown for a line across the center of the model at 10 km parallel to strike. Zero on the horizontal axis corresponds to the surface trace of the fault. Negative distances correspond to the footwall and positive distances correspond to the hanging wall. The ground motion is consistent with the fault motion of Figure 11.

Zeng, Y., B. Shi, and J. N. Brune (1997). Dynamic simulation of shallow angle thrust faulting, *EOS Trans. AGU* **77,** Fall Meeting Supplement, 505.

Institute for Crustal Studies and Department of Geological Sciences
University of California
Santa Barbara, CA 93106
(D. D. O., R. J. A.)

Institute for Crustal Studies and Materials Research Laboratory
University of California
Santa Barbara, CA 93106
(S. B. N.)

Manuscript received 9 August 1999.